ChemPubSoc Europe

DOI: 10.1002/cctc.201500009

CHEMCATCHEM
Full Papers

Promoting Visible-Light Photocatalysis with Palladium Species as Cocatalyst

Xiuzhen Li,[a, b] Nan Zhang,[a, b] and Yi-Jun Xu*[a, b]

Conventionally, Pd catalysis has been widely used in either heterogeneous or homogeneous thermocatalytic organic synthesis. Herein, we demonstrate a case study on the important, cocatalyst role of Pd nanoparticles in ternary In_2S_3–(reduced graphene oxide–palladium) [In_2S_3–(RGO–Pd)] composites for the selective oxidation of alcohols under visible-light irradiation. Pd acts as dual cocatalyst along with RGO to promote the more efficient separation of photogenerated electron–hole pairs and facilitate their spatial transfer across the interface in ternary In_2S_3–(RGO–Pd) composites, which leads to higher activity than that of binary In_2S_3–RGO composites. This work highlights the promising scope of using Pd nanoparticles as a cocatalyst for promoting visible-light photocatalysis towards selective organic transformations under ambient conditions.

Introduction

Since the 1960s, Pd catalysis has garnered much attention in the field of organic synthesis owing to the compatibility of Pd with an extensive range of functionalities and the feasibility to selectively functionalize cyclopalladated intermediates.[1–10] Thus far, Pd-based catalysts (Pd^0 and Pd^{II} complexes) have been used for a plethora of organic reactions, such as Heck reactions, Negishi reactions, Suzuki reactions, C–H functionalization reactions, and cross-coupling reactions, which provide access to agrochemicals, pharmaceutical intermediates, polymer precursors, fragrances, hormones, and many other valued chemical products.[2,4–24]

In addition to the versatility of Pd catalysts in conventional thermocatalysis, Pd nanoparticles have been found to act as electron reservoirs in the photocatalytic systems for solar energy conversion.[25–28] Solar-driven photocatalytic energy conversion particularly based on heterogeneous semiconductors is becoming a hot topic on account of its potential for solving environmental and energy problems in a sustainable way, which are the biggest challenges of the 21st century.[29–34] Despite the notable advances in the application of common TiO_2-based photocatalysts, the low quantum efficiency resulting from the high recombination of photogenerated electron–hole pairs and the wide bandgap of TiO_2 limit their practical photocatalytic application on a large scale.[27,34–40]

Graphene (GR), an electron conductive 2D platform, has been used as a cocatalyst to improve the lifetime and transfer efficiency of charge carriers photogenerated from semiconductors upon light irradiation, thereby enhancing the photoactivity of semiconductors.[41–48] In view of the electron conductive property of the 2D platform of GR and the intrinsically low-lying Fermi energy level of noble metal Pd nanoparticles,[36,49] integrating the respective advantages of these two components in a photocatalytic system used as dual cocatalysts is expected to enhance the photocatalytic activity of semiconductors by facilitating the spatial charge carriers transfer across the interface in the composites.

Herein, we choose In_2S_3, a typical III–VI group sulfide with desirable visible-light response,[50–53] to fabricate ternary In_2S_3–(RGO–Pd) composites with Pd nanoparticles and reduced graphene oxide (RGO), the most common type of GR used to construct photocatalysts, as cocatalysts through a wet chemistry method. Taking selective oxidation of alcohols as a probing reaction, which is a significant transformation of great industrial importance owing to the wide use of the products (e.g., aldehyde and ketone derivatives) in fragrance, confectionery, and pharmaceutical industries, the In_2S_3–(RGO–Pd) composites exhibit enhanced activity upon visible-light irradiation as compared with the optimal binary In_2S_3–RGO composite and blank In_2S_3. This result is ascribed to the fact that Pd nanoparticles, located in the interfacial layer between In_2S_3 and RGO, act as dual cocatalyst with RGO to facilitate spatial charge carriers transfer across the interface in ternary In_2S_3–(RGO–Pd) composites. This case study highlights the promising scope of using Pd nanoparticles as a cocatalyst for promoting visible-light photocatalysis towards selective organic transformations under ambient conditions.

---

[a] *X. Li, N. Zhang, Prof. Y.-J. Xu*
State Key Laboratory of Photocatalysis on Energy and Environment
College of Chemistry
Fuzhou University
Fuzhou 350002 (P.R. China)
E-mail: yjxu@fzu.edu.cn

[b] *X. Li, N. Zhang, Prof. Y.-J. Xu*
College of Chemistry
New Campus
Fuzhou University
Fuzhou 350108 (P.R. China)

Supporting information for this article is available on the WWW under http://dx.doi.org/10.1002/cctc.201500009.

Part of a Special Issue on Palladium Catalysis. A link to the Table of Contents will appear here once the Special Issue is assembled.

Results and Discussion

Ternary In_2S_3–(RGO–Pd) composites with different weight addition ratios of RGO–Pd have been prepared by using a facile solution approach (Scheme 1). First, we anchor Pd nanoparticles onto the surface of the graphene oxide (GO) sheet via a one-step clean strategy without the addition of the surfactant, during which the redox reaction between $PdCl_4^{2-}$ and GO occurs.[62,63] After this step, GO–Pd still maintains abundant surface oxygen-containing functional groups (Figure S1), which provides a flexible platform for the introduction of a third component to fabricate ternary composites. Thus, In_2S_3 can be assembled on the GO–Pd surface by using the "structure-directing" property of GO through a facile hydrothermal process during which GO is sufficiently reduced to RGO to form the final ternary In_2S_3–(RGO–Pd) composites.

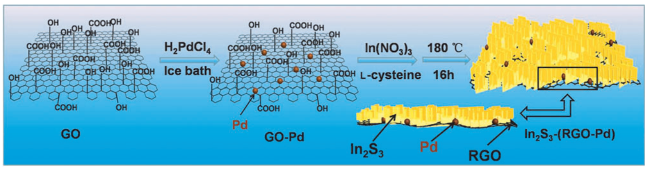

Scheme 1. Schematic illustration of the preparation of ternary In_2S_3–(RGO–Pd) composites by using a facile, wet chemistry method.

Field-emission SEM (FESEM) is used to provide the information on the morphology of blank In_2S_3, binary In_2S_3–1 %RGO composite, and ternary In_2S_3–1 %(RGO–Pd) composite, which exhibit the optimal photoactivity (see below). Without the addition of GO or GO–Pd, blank In_2S_3 has a flowerlike structure with a mean diameter of 1 µm (Figure 1 A). As for the optimal binary In_2S_3–1 %RGO composite, irregular petal-like In_2S_3 grows compactly along the RGO mat platform (Figure 1 B). Notably, the ternary In_2S_3–1 %(RGO-Pd) composite shows a morphology similar to that of the optimal binary In_2S_3–1 %RGO composite (Figure 1 C). This suggests that the addition of a small amount of Pd nanoparticles to the ternary In_2S_3–(RGO–Pd) composite almost has no effect on its morphology as compared with the morphology of the binary In_2S_3–RGO composite.

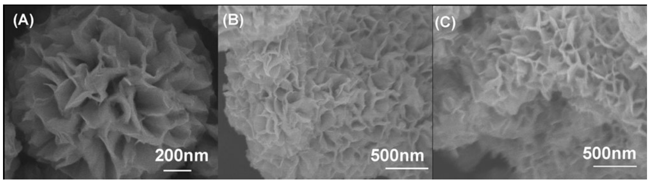

Figure 1. Typical FESEM images of A) blank In_2S_3, B) In_2S_3–1 %RGO composite, and C) ternary In_2S_3–1 %(RGO–Pd) composite.

To further verify the microscopic structure of the ternary In_2S_3–(RGO–Pd) composite, TEM analysis has been performed (Figure 2). As shown in Figure 2 A and B, irregular petal-like In_2S_3 has grown compactly onto the RGO sheet, which is similar to the morphology of the binary In_2S_3–1 %RGO composite (Figure S2). This observation is in accordance with the SEM results elaborated above. Lattice fringe can be clearly seen in the high-resolution TEM image shown in Figure 2 C. The spacing is measured to be 0.324 nm, which can be indexed to the (311) crystal face of the cubic β-In_2S_3 phase. And the lattice spacing of 0.226 nm corresponds to the (111) face of cubic Pd, which indicates the successful introduction of Pd nanoparticles into ternary In_2S_3–(RGO–Pd) composites. Meanwhile, the existence of Pd nanoparticles can be indirectly confirmed by the TEM image and X-ray photoelectron spectrum (XPS) of GO–Pd. The TEM image of GO–Pd (Figure S3) shows that Pd nanoparticles are well dispersed on the GO surface with a narrow size distribution at approximately 0.5–3 nm. As shown in Figure S4, the Pd 3d XPS spectrum of GO–Pd consists of two typical peaks at approximately 335.4 and 340.6 eV, which can be, respectively, indexed to Pd $3d_{5/2}$ and Pd $3d_{3/2}$ core levels of Pd. The selected area electron diffraction image (Figure 2 D) shows the polycrystalline structure of the In_2S_3–1 %(RGO–Pd) composite. The diffraction rings (pointed by the arrow) can be, respectively, indexed to (311), (400), and (400) planes of the cubic β-In_2S_3 phase. These results indicate that the addition of Pd nanoparticles does not have a significant effect on the morphological structure of the ternary In_2S_3–(RGO–Pd) composite as compared with the binary In_2S_3–1 %RGO composite.

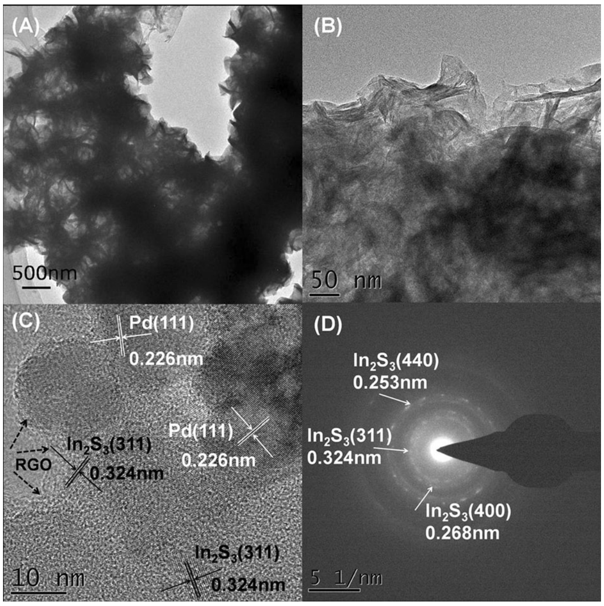

Figure 2. A and B) TEM images, C) high-resolution TEM image, and D) selected area electron diffraction pattern of the as-synthesized ternary In_2S_3–1 %(RGO–Pd) composite.

The XRD patterns of ternary In_2S_3–(RGO–Pd) composites with different weight addition ratios of RGO–Pd and blank In_2S_3 are shown in Figure 3. All the samples show similar XRD patterns that can be indexed to the cubic β-In_2S_3 phase (JCPDS card no. 32-0456). The peaks located at approximately 14.2, 20.9, 27.4, 28.7, 33.2, and 47.7° can be, respectively, ascribed to the (111), (211), (311), (222), (400), and (440) crystal planes of the cubic β-In_2S_3 phase.[50,51,53] The XRD patterns of ternary In_2S_3–(RGO–Pd) composites are similar to those of binary In_2S_3–RGO

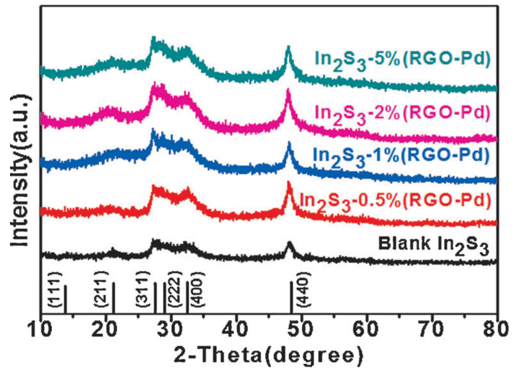

Figure 3. XRD spectra of the as-synthesized ternary In_2S_3–(RGO–Pd) composites with different weight addition ratios of RGO–Pd and blank In_2S_3.

composites with different weight addition ratios of RGO–Pd (Figure S5); this finding indicates that the addition of Pd nanoparticles has little effect on the crystalline structure of In_2S_3. No apparent peaks for Pd nanoparticles are detected, which can be probably ascribed to the relatively low amount of Pd nanoparticles added to the ternary composites. No obvious diffraction peaks of RGO can be found because of two possible reasons: 1) the disappearance of the layer stacking regularity after the redox reaction of graphite and 2) the relatively low diffraction intensity of RGO at 26.0° might be shielded by the main peak of In_2S_3 at 27.4°.[45,55,60,61,66]

The UV/Vis diffuse reflectance spectra (DRS) for characterization of the optical properties of the samples are displayed in Figure 4. It can be found that the absorption intensity in the visible-light region (500–800 nm) strengthens with the increase in the amount of RGO–Pd, which is possibly due to the intrinsic absorption of black RGO.[45,55] Such a phenomenon is also observed for binary In_2S_3–RGO composites (Figure S6), which indicates that the introduction of Pd nanoparticles does not have a great effect on the optical properties of ternary In_2S_3–(RGO–Pd) composites as compared with binary In_2S_3–RGO composites. From the above results, it can be concluded that the ternary In_2S_3–(RGO–Pd) and binary In_2S_3–RGO composites show analogous morphology, crystalline phase, and optical properties, which provides a basic framework to study the possible role of Pd nanoparticles in affecting the photocatalytic performance of ternary In_2S_3–(RGO–Pd) and binary In_2S_3–RGO composites.

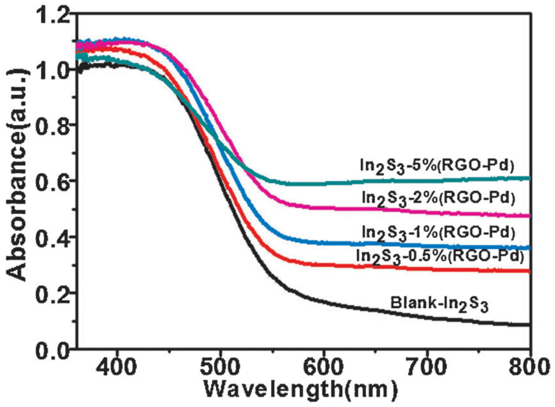

Figure 4. UV/Vis diffuse reflectance spectra of ternary In_2S_3–(RGO–Pd) composites with different weight addition ratios of RGO–Pd and blank In_2S_3.

The catalytic activity of ternary In_2S_3–(RGO–Pd) composites is initially estimated by the selective oxidation of benzyl alcohol to benzaldehyde under visible-light irradiation ($\lambda > 420$ nm). Blank In_2S_3 and In_2S_3–1%RGO composite with optimal activity for the selective oxidation of benzyl alcohol among binary In_2S_3–RGO composites (Figure S7) have been used as reference samples. With the addition of a small amount of Pd nanoparticles, the conversion of benzyl alcohol and yield for the target product benzaldehyde over ternary In_2S_3–(RGO–Pd) composites are significantly increased as compared with the optimal binary In_2S_3–1%RGO composite and blank In_2S_3, and the In_2S_3–1%(RGO–Pd) composite shows the optimal photocatalytic activity among all ternary In_2S_3–(RGO–Pd) composites (Figure 5).

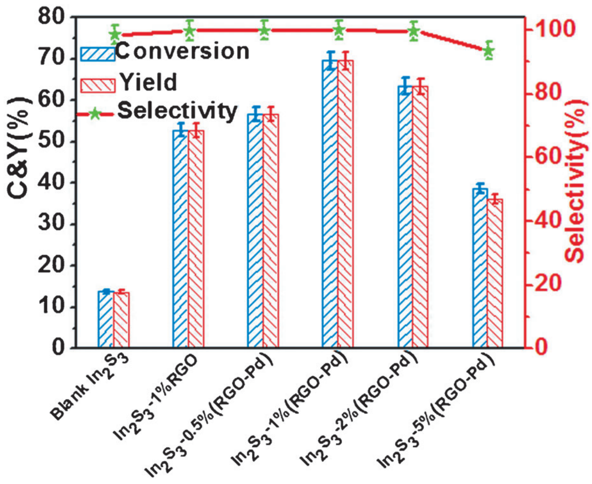

Figure 5. Photocatalytic selective oxidation of benzyl alcohol to benzaldehyde over ternary In_2S_3–(RGO–Pd) composites with different weight addition ratios of RGO–Pd, In_2S_3–1%RGO composite, and blank In_2S_3 under visible-light irradiation ($\lambda > 420$ nm) for 2 h. C&Y = Conversion and yield.

Notably, as the weight addition ratio of RGO–Pd reaches 5%, both activity and selectivity decrease, which could be due to the lowered contact of the surface of semiconductor In_2S_3 with light irradiation in the ternary In_2S_3–5%(RGO–Pd) composite; this has also been observed in previous works.[43,61,66,68] Another reason for the decrease in selectivity is that the target product benzaldehyde may not be timely and easily desorbed from the surface of photocatalysts owing to the strong adsorption ability of the carbon material RGO with relatively higher addition in ternary In_2S_3–(RGO–Pd) composites. Under this circumstance, deep oxidation of benzaldehyde may occur, thereby resulting in decrease in selectivity.[43,66,68]

To exclude the possible contribution of RGO and/or Pd nanoparticles to the enhanced photoactivity of the In_2S_3–(RGO–Pd) composite as compared with blank In_2S_3 and the optimal binary In_2S_3–RGO composite, the activity of RGO–Pd for the selective oxidation of benzyl alcohol has also been evaluated with or without visible-light irradiation. The results presented in Figure S8 indicate that RGO–Pd exhibits quite poor activity at ambient conditions under both dark and visible-light illumination, which suggests that in ternary In_2S_3–(RGO–Pd) composites, the active component is In_2S_3 and the roles of Pd nanoparticles and RGO serve as cocatalysts.

Time-online profiles for the selective oxidation of benzyl alcohol further confirm the enhanced activity of the In_2S_3–1 %(RGO–Pd) photocatalyst as compared with both the optimal binary In_2S_3–1 %RGO composite and blank In_2S_3. As shown in Figure 6, the conversion of benzyl alcohol and yield of benzaldehyde obtained over the samples increase gradually with the increase in irradiation time and the enhanced photoactivity of the In_2S_3–1 %(RGO–Pd) composite compared with the In_2S_3–1 %RGO composite and blank In_2S_3 is obvious. To confirm this superiority of the In_2S_3–1 %(RGO–Pd) composite, the selective oxidation of other benzylic alcohols and allylic alcohols to corresponding aldehydes over the samples has also been investigated under visible-light irradiation. The photocatalytic performance of the In_2S_3–1 %(RGO–Pd) composite evidently outperforms that of the In_2S_3–1 %RGO composite and blank In_2S_3 in all selected reaction systems (Table S1).

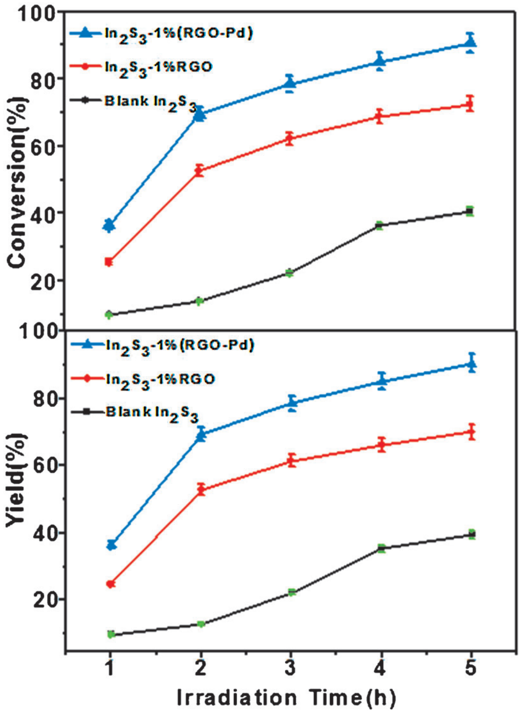

Figure 6. Time-online photocatalytic selective oxidation of benzyl alcohol to benzaldehyde over the as-prepared ternary In_2S_3–1 %(RGO–Pd) composite, In_2S_3–1 %RGO composite, and blank In_2S_3 under visible-light irradiation ($\lambda > 420$ nm).

The above results indicate that the introduction of Pd nanoparticles into the interlayer matrix of In_2S_3 and RGO can improve the visible-light photocatalytic performance of In_2S_3–(RGO–Pd) composites for the selective aerobic oxidation of alcohols. To understand and explore the origin of the enhanced photocatalytic activity of In_2S_3–(RGO–Pd) composites for the selective oxidation of alcohols as compared with the optimal binary In_2S_3–1 %RGO composite and blank In_2S_3, relevant characterizations have been performed. The photoluminescence (PL) spectra provide the information about surface processes concerning the fate of charge carriers photogenerated from semiconductors.[40,55,69–71] As displayed in Figure 7, the PL intensity observed for the In_2S_3–1 %(RGO–Pd) composite is weaker than that observed for both the optimal binary In_2S_3–1 %RGO composite and blank In_2S_3 at the excitation wavelength of 420 nm, which indicates the more efficient inhibition of the recombination of electron–hole pairs photogenerated in the In_2S_3–1 %(RGO-Pd) composite. This increased lifetime of photogenerated charge carriers plays a crucial role in improving the photocatalytic performance of the In_2S_3–1 %(RGO–Pd) composite as compared with that of both In_2S_3–1 %RGO composite and blank In_2S_3. Thus, we can assume that the introduction of Pd nanoparticles facilitates the transfer of electrons and suppresses the recombination of charge carriers, which thus leads to the enhancement of photoactivity of ternary In_2S_3–(RGO–Pd) composites.

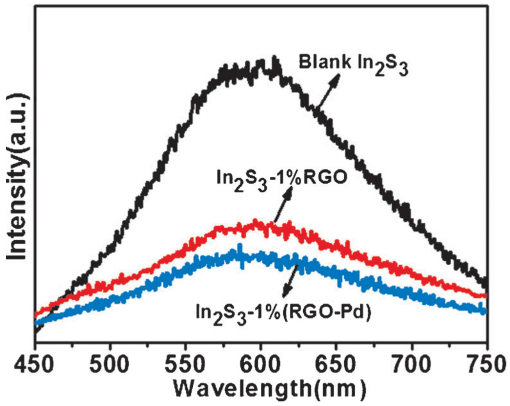

Figure 7. PL spectra of the ternary In_2S_3–1 %(RGO–Pd) composite, In_2S_3–1 %RGO composite, and blank In_2S_3 at an excitation wavelength of 420 nm.

To further identify the role of Pd nanoparticles in ternary In_2S_3–(RGO–Pd) composites in enhancing the photoactivity, the transient photocurrent density for In_2S_3–1 %(RGO–Pd) composite, In_2S_3–1 %RGO composite, and blank In_2S_3 electrodes was measured in the electrolyte of 0.2 M Na_2SO_4 aqueous solution without bias versus Ag/AgCl under visible-light irradiation ($\lambda >$ 420 nm). As shown in Figure 8 A, the photocurrent density of the In_2S_3–1 %(RGO–Pd) composite under visible-light irradiation ($\lambda > 420$ nm) is higher than that of both In_2S_3–1 %RGO composite and blank In_2S_3, which implies that the electron transfer is more efficient in the ternary In_2S_3–1 %(RGO–Pd) composite. Moreover, electrochemical impedance spectroscopy (EIS) has been performed to study the migration of charge carriers in electrode materials.[72] From the EIS Nyquist plots of the In_2S_3–1 %(RGO–Pd) composite, In_2S_3–1 %RGO composite, and blank In_2S_3 electrode materials cycled in 0.5 M KCl aqueous solution containing 0.01 M $K_3[Fe(CN)_6]/K_4[Fe(CN)_6]$ (Figure 8 B), we can

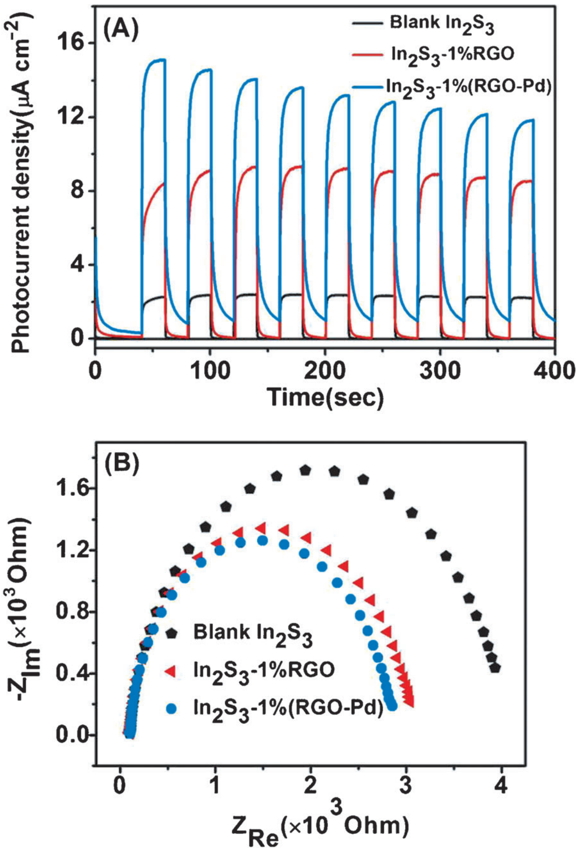

Figure 8. A) Transient photocurrent density without bias versus Ag/AgCl and B) EIS Nyquist plots of the as-prepared ternary In_2S_3–1 %(RGO–Pd) composite, In_2S_3–1 %RGO composite, and blank In_2S_3 electrodes on the FTO substrate.

see that all the samples show semicycles at high frequencies that are related to the resistance of the electrodes.[72,73] The plot of the ternary In_2S_3–1 %(RGO–Pd) composite shows more depressed semicircles at high frequencies corresponding to the more efficient charge carrier transfer as compared with the plots of In_2S_3–1 %RGO composite and blank In_2S_3. These results indicate that Pd nanoparticles introduced into the interfacial layer matrix of In_2S_3 and RGO act as dual cocatalyst with RGO to improve the lifetime of photogenerated charge carriers and the transfer efficiency of charge carriers across the interface between semiconductor In_2S_3 and RGO sheets, which leads to the enhanced photoactivity of ternary In_2S_3–(RGO–Pd) composites.

In addition, the surface area and porosity have been investigated for the samples. The N_2 adsorption–desorption isotherms of the In_2S_3–1 %(RGO–Pd) composite, In_2S_3–1 %RGO composite, and blank In_2S_3 exhibit type IV isotherm with H_3-type hysteresis loop, which is characteristic of mesoporous solids according to the IUPAC classification (Figure S9).[67] The specific surface area and pore volume for the In_2S_3–1 %(RGO–Pd) composite are measured to be approximately 32 m^2g^{-1} and 0.19 cm^3g^{-1}, respectively, which are larger than those of blank In_2S_3 ($\approx$18 m^2g^{-1} and 0.11 cm^3g^{-1}) and similar to those of the In_2S_3–1 %RGO composite ($\approx$37 m^2g^{-1} and 0.23 cm^3g^{-1}) (Table S2). These results indicate that the introduction of Pd nanoparticles does not have a significant effect on the surface area and porosity of ternary In_2S_3–(RGO–Pd) composites as compared with binary In_2S_3–RGO composites. Besides, adsorption experiments of alcohols in the dark have been performed. There is almost no difference in adsorptivity between the In_2S_3–1 %RGO composite and the In_2S_3–1 %(RGO–Pd) composite, although they show higher adsorptivity than did blank In_2S_3 (Figure S10). Therefore, the enhanced photoactivity of the In_2S_3–1 %(RGO–Pd) composite compared with the optimal binary In_2S_3–1 %RGO composite cannot be attributed to the difference in surface area and porosity.

Furthermore, to understand the role of Pd nanoparticles in the reaction mechanism for the photocatalytic performance of In_2S_3–(RGO–Pd) composites, controlled experiments with addition of various radical scavengers for the photocatalytic selective oxidation of benzyl alcohol in the benzotrifluoride (BTF) solvent have been performed.[45,74,75] When the radical scavengers of ammonium oxalate (AO) for photogenerated holes, potassium persulfate ($K_2S_2O_8$) for electrons, and benzoquinone (BQ) for superoxide radicals ($O_2^{\cdot -}$) are added respectively, the conversion of benzyl alcohol over the optimal ternary In_2S_3–1 %(RGO-Pd) composite, optimal binary In_2S_3–1 %RGO composite, and blank In_2S_3 is inhibited (Figure 9). The controlled experiment with the addition of *tert*-butyl alcohol (TBA) as the radical scavenger for hydroxyl radicals (·OH) shows that there is almost no change in the conversion of benzyl alcohol. This result is in agreement with the previous reports that no hydroxyl radicals are formed in the BTF solvent.[61,64,66,76] Hence, for the visible-light photocatalytic selective oxidation of benzyl alcohol over the ternary In_2S_3–1 %(RGO–Pd) composite, optimal binary In_2S_3–1 %RGO composite, and blank In_2S_3, the primary active radical species are photogenerated holes, electrons, and activated oxygen (e.g., $O_2^{\cdot -}$).

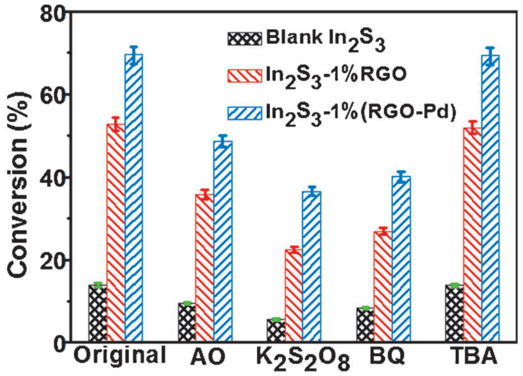

Figure 9. Controlled experiments with different radical scavengers for the photocatalytic selective oxidation of benzyl alcohol over the ternary In_2S_3–1 %(RGO–Pd) composite, In_2S_3–1 %RGO composite, and blank In_2S_3 in the BTF solvent under visible-light irradiation ($\lambda > 420$ nm) for 2 h; AO is a scavenger for photogenerated holes, $K_2S_2O_8$ for photogenerated electrons, BQ for superoxide radicals, and TBA for hydroxyl radicals.

The photocatalytic stability of the optimal In_2S_3–1 %(RGO–Pd) composite has also been evaluated. No apparent activity loss is observed for the selective aerobic oxidation of benzyl alcohol in the BTF solvent under visible-light irradiation over the In_2S_3–1%(RGO–Pd) composite after four successive recycles, which indicates that the In_2S_3–1%(RGO–Pd) composite is able to serve as a stable and reusable visible-light photocatalyst for the selective oxidation of a series of alcohols under controlled reaction conditions (Figure S11).

According to the above discussion, the enhancement of the photoactivity of ternary In_2S_3–(RGO–Pd) composites can be primarily attributed to the introduction of Pd nanoparticles into the interlayer matrix of In_2S_3 and RGO that act as dual cocatalyst with RGO, which thus leads to the optimization of the separation and spatial transfer of charge carriers across the interface in ternary In_2S_3–(RGO–Pd) composites. A possible reaction mechanism has been proposed for the photocatalytic oxidation of alcohols over ternary In_2S_3–(RGO–Pd) composites (Scheme 2). There are two thermodynamically possible routes of electron transfer in ternary In_2S_3–(RGO–Pd) composites. One is that the electrons can transfer from the conduction band (CB) of semiconductor In_2S_3 (−0.8 V vs. normal hydrogen electrode, NHE) to Pd nanoparticles with large work function (+0.62 V vs. NHE)[77] as an electron reservoir. The other is that the electrons photogenerated from the conduction band of In_2S_3 can transfer to RGO sheets (its work function is −0.08 V vs. NHE) and then to Pd nanoparticles for their matchable band structure and close interfacial contact. In this way, the respective advantages of both RGO and Pd in a photocatalytic system used as dual cocatalysts is expected to enhance the photocatalytic activity of semiconductors by spatially boosting the charge carriers relay among the composites system as compared to their binary In_2S_3–RGO counterparts.

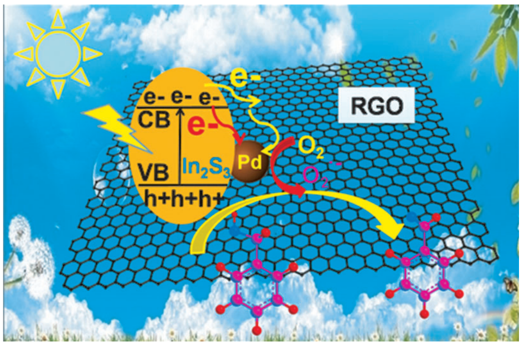

Scheme 2. Schematic diagram of the charge carrier transfer and proposed mechanism for the selective oxidation of alcohols to aldehydes over ternary In_2S_3–(RGO–Pd) composites under visible-light irradiation.

Conclusions

In summary, we have synthesized ternary In_2S_3–(RGO–Pd) composites by using a facile wet chemistry method. Metallic Pd nanoparticles, embedded in the interfacial layer between In_2S_3 and RGO, can act as dual cocatalyst with RGO to facilitate spatial charge carriers transfer across the interface in ternary In_2S_3–(RGO–Pd) composites, which thus leads to the enhanced activity of In_2S_3–(RGO–Pd) composites for the selective aerobic oxidation of alcohols upon visible-light irradiation as compared with that of the optimal binary In_2S_3–RGO composite and blank In_2S_3. This work highlights the promising scope of using Pd nanoparticles as a cocatalyst for promoting visible-light photocatalysis towards selective organic transformations under ambient conditions.

Experimental Section

Materials

Indium(III) nitrate hydrate ($In(NO_3)_3{\cdot}4.5H_2O$), L-cysteine ($C_3H_7NO_2S$), graphite powder, sulfuric acid (H_2SO_4), nitric acid (HNO_3), hydrochloric acid (HCl), sodium hydroxide (NaOH), potassium persulfate ($K_2S_2O_8$), phosphorus pentoxide (P_2O_5), potassium permanganate ($KMnO_4$), hydrogen peroxide 30% (H_2O_2), ethanol (C_2H_6O), palladium chloride ($PdCl_2$), benzyl alcohol (C_7H_8O), ammonium oxalate ($N_2H_8C_2O_4$, AO), benzoquinone ($C_6H_4O_2$, BQ), and *tert*-butyl alcohol ($C_4H_{10}O$, TBA) were supplied by Sinopharm chemical reagent Co., Ltd. (Shanghai, China). Benzotrifluoride ($C_7H_5F_3$, BTF), 4-methylbenzyl alcohol ($C_8H_{10}O$), 4-methoxybenzyl alcohol ($C_8H_{10}O_2$), 4-nitrobenzyl alcohol ($C_7H_7NO_3$), 4-chlorobenzyl alcohol (C_7H_7OCl), 4-fluorobenzyl alcohol (C_7H_7OF), cinnamyl alcohol ($C_9H_{10}O$), and 3-methyl-2-buten-1-ol ($C_5H_{10}O$) were purchased from Alfa Aesar Co., Ltd. (Tianjin, China). All the chemicals were analytical grade and used without further purification. The deionized water was from local sources.

Synthesis

Synthesis of GO

Natural graphite powder was used to synthesize GO by using a modified Hummers method that was presented in our previous works as well.[45,54–61] The details of the preparation procedure are given in the Supporting Information.

Preparation of GO–Pd composite

The GO–Pd composite was prepared by using a facile, one-step clean strategy.[62,63] Typically, GO (30 mg) was fully dispersed in deionized water (60 mL). The H_2PdCl_4 solution (10 mM, 3.13 mL) was added dropwise to the homogeneous GO solution. The mixture was stirred in ice bath for 30 min. Then, the resulting mixture was centrifuged at 12 000 rpm for 30 min. The collected solid was washed with deionized water until the ion concentration of the supernatant was less than 10 ppm. After drying the supernatant overnight at 60 °C in an electric oven, the GO–Pd composite was obtained.

Fabrication of In_2S_3–(RGO–Pd) composites with different weight addition ratios of RGO–Pd

The given amount of the as-prepared GO–Pd composite was dispersed ultrasonically in distilled water (40 mL) and mixed with indium(III) nitrate hydrate (0.5 mmol). After stirring the mixture for 0.5 h, L-cysteine (2 mmol) was added to it under vigorous stirring. Then, pH was adjusted to 8 by adding sodium hydroxide (1 M) dropwise. After stirring for 1 h, the mixture was transferred into a 50 mL Teflon-lined stainless steel autoclave, which was sealed and treated at 180 °C for 16 h. Subsequently, the as-synthesized products were separated by centrifugation and washed thrice and twice with distilled water and absolute ethanol, respectively. After drying the products at 60 °C for 6 h, the target products were obtained.

Preparation of In_2S_3–RGO composite and blank In_2S_3

For comparison, the In_2S_3–RGO composite and blank In_2S_3 were also fabricated by using the same hydrothermal process as that of In_2S_3–(RGO–Pd) composites with GO instead of GO–Pd and without GO, respectively.

Characterization

The XRD patterns of the samples were recorded on a Bruker D8 Advance X-ray diffractometer with CuK_α radiation at 40 kV and 40 mA and $2\theta = 10–80^\circ$ (scan rate: $0.02^\circ s^{-1}$). UV/Vis diffuse reflectance spectroscopy (DRS) was used to characterize the optical properties of the samples with a UV/Vis spectrophotometer (Varian Cary 500) with $BaSO_4$ as a reference material. FESEM was used to determine the morphology of the samples on a FEI Nova NanoSEM 230 spectrophotometer. TEM analysis was performed with a JEOL JEM 2010 EX instrument operating at an accelerating voltage of 200 kV. X-ray photoelectron spectroscopy (XPS) analysis was performed with a Thermo Scientific ESCALAB 250 X-ray photoelectron spectrometer with monochromatic AlK_α as the X-ray source, a hemispherical analyzer, and a sample stage with multiaxial adjustability to obtain the surface composition of the as-obtained samples. All the binding energies were calibrated by the C 1s peak at 284.6 eV. The PL spectra were recorded with an Edinburgh FL/FS900 spectrophotometer at an excitation wavelength of 420 nm. Nitrogen adsorption–desorption isotherms and BET specific surface areas were obtained with Micromeritics ASAP 2010 system. The photoelectrochemical analysis was performed with a homemade three-electrode cell. A Pt plate was used as the counterelectrode, and an Ag/AgCl electrode was used as the reference electrode. The electrolyte was the Na_2SO_4 aqueous solution (0.2 M) without an additive (pH 6.8). The working electrode was prepared on fluorine-doped tin oxide (FTO) glass that was sonicated in ethanol and dried at 80 °C before use. The boundary of FTO glass was protected with the Scotch tape. The sample (2 mg) was adequately dispersed in DMF (0.5 mL, Sinopharm Chemical Reagent Co., Ltd.) through sonication. The as-obtained slurry was spread onto the pretreated FTO glass. After air drying, the working electrode was further dried at 393 K for 2 h to improve adhesion. Then, the Scotch tape was removed, and the uncoated part of the electrode was isolated with epoxy resin. The visible-light irradiation source was a 300 W Xe arc lamp system equipped with a UV-cut filter ($\lambda > 420$ nm). The EIS experiments were performed with a CHI-660D workstation (CH Instruments) in the electrolyte of KCl aqueous solution (0.5 M) containing $K_3[Fe(CN)_6]/K_4[Fe(CN)_6]$ (0.01 M, 1:1) under open circuit potential conditions.

Catalytic activity

The photocatalytic selective oxidation of a series of alcohols was performed as described in previous works.[45,61,64–66] Typically, alcohol (0.1 mmol) and the as-synthesized catalyst (8 mg) were suspended in BTF (1.5 mL), which was saturated with molecular oxygen. Subsequently, this mixture was transferred into a 10 mL Pyrex glass bottle, which was filled with molecular oxygen at a pressure of 0.1 MPa and stirred for 20 min to establish the adsorption–desorption equilibrium. The mixture was irradiated by a 300 W Xe arc lamp (PLS-SXE-300, Beijing Perfect light Co., Ltd.) with a UV-cut filter to cut off light with a wavelength less than 420 nm. Then, the mixture was centrifuged at 12 000 rmp for 10 min to remove the catalyst particles. The remaining solution was analyzed with an Agilent 7820A gas chromatograph. Conversion of alcohol, yield, and selectivity of the aldehyde were calculated by using Equations (1)–(3):

$$\text{Conversion}\ (\%) = \frac{C_0 - C_r}{C_0} \times 100 \tag{1}$$

$$\text{Yield}\ (\%) = \frac{C_p}{C_0} \times 100 \tag{2}$$

$$\text{Selectivity}\ (\%) = \frac{C_p}{C_0 - C_r} \times 100 \tag{3}$$

in which C_0 is the initial concentration of alcohol and C_r and C_p are the concentrations of the substrate alcohol and the corresponding product aldehyde, respectively, at a certain time after the photocatalytic reaction.

Acknowledgements

We gratefully acknowledge support from the Key Project of National Natural Science Foundation of China (U1463204), the National Natural Science Foundation of China (20903023 and 21173045), the Award Program for Minjiang Scholar Professorship, the Natural Science Foundation of Fujian Province for Distinguished Young Investigator Grant (2012J06003), and the Program for Returned High-Level Overseas Chinese Scholars of Fujian province.

Keywords: alcohols · graphene · oxidation · palladium · photocatalysis

[1] E.-i. Negishi, L. Anastasia, *Chem. Rev.* **2003**, *103*, 1979–2018.
[2] J. A. Marshall, *Chem. Rev.* **2000**, *100*, 3163–3186.
[3] G. Zeni, R. C. Larock, *Chem. Rev.* **2004**, *104*, 2285–2310.
[4] C. Amatore, A. Jutand, *Acc. Chem. Res.* **2000**, *33*, 314–321.
[5] I. P. Beletskaya, A. V. Cheprakov, *Chem. Rev.* **2000**, *100*, 3009–3066.
[6] R. F. Heck, *Acc. Chem. Res.* **1979**, *12*, 146–151.
[7] N. Miyaura, A. Suzuki, *Chem. Rev.* **1995**, *95*, 2457–2483.
[8] K. Nicolaou, P. G. Bulger, D. Sarlah, *Angew. Chem. Int. Ed.* **2005**, *44*, 4442–4489; *Angew. Chem.* **2005**, *117*, 4516–4563.
[9] R. Zimmer, C. U. Dinesh, E. Nandanan, F. A. Khan, *Chem. Rev.* **2000**, *100*, 3067–3126.
[10] S. Cacchi, G. Fabrizi, *Chem. Rev.* **2005**, *105*, 2873–2920.
[11] B. M. Trost, D. L. Van Vranken, *J. Am. Chem. Soc.* **1993**, *115*, 444–458.
[12] T. Nishimura, S. Uemura, *J. Am. Chem. Soc.* **2000**, *122*, 12049–12050.
[13] B. M. Trost, J. Dumas, M. Villa, *J. Am. Chem. Soc.* **1992**, *114*, 9836–9845.
[14] T. Okazawa, T. Satoh, M. Miura, M. Nomura, *J. Am. Chem. Soc.* **2002**, *124*, 5286–5287.
[15] A. F. Littke, G. C. Fu, *Angew. Chem. Int. Ed.* **2002**, *41*, 4176–4211; *Angew. Chem.* **2002**, *114*, 4350–4386.
[16] S. Kim, J. Jackiw, E. Robinson, K. S. Schanze, J. R. Reynolds, J. Baur, M. F. Rubner, D. Boils, *Macromolecules* **1998**, *31*, 964–974.
[17] T. W. Lyons, M. S. Sanford, *Chem. Rev.* **2010**, *110*, 1147–1169.
[18] N. A. Bumagin, E. V. Luzikova, *J. Organomet. Chem.* **1997**, *532*, 271–273.
[19] J. Ruan, O. Saidi, J. A. Iggo, J. Xiao, *J. Am. Chem. Soc.* **2008**, *130*, 10510–10511.

[20] D. W. Old, J. P. Wolfe, S. L. Buchwald, *J. Am. Chem. Soc.* **1998**, *120*, 9722–9723.
[21] R. F. Heck, J. P. Nolley, *J. Org. Chem.* **1972**, *37*, 2320–2322.
[22] N. E. Leadbeater, M. Marco, *Org. Lett.* **2002**, *4*, 2973–2976.
[23] R. Martin, S. L. Buchwald, *Acc. Chem. Res.* **2008**, *41*, 1461–1473.
[24] N. Miyaura, T. Yanagi, A. Suzuki, *Synth. Commun.* **1981**, *11*, 513–519.
[25] J. Papp, H. S. Shen, R. Kershaw, K. Dwight, A. Wold, *Chem. Mater.* **1993**, *5*, 284–288.
[26] C. Belver, M. a. J. López-Muñoz, J. M. Coronado, J. Soria, *Appl. Catal. B* **2003**, *46*, 497–509.
[27] X. Pan, Y.-J. Xu, *J. Phys. Chem. C* **2013**, *117*, 17996–18005.
[28] X. Pan, Y.-J. Xu, *ACS Appl. Mater. Interfaces* **2014**, *6*, 1879–1886.
[29] M. A. Fox, M. T. Dulay, *Chem. Rev.* **1993**, *93*, 341–357.
[30] F. Wen, C. Li, *Acc. Chem. Res.* **2013**, *46*, 2355–2364.
[31] A. Mills, R. H. Davies, D. Worsley, *Chem. Soc. Rev.* **1993**, *22*, 417–425.
[32] W. Fan, Q. Zhang, Y. Wang, *Phys. Chem. Chem. Phys.* **2013**, *15*, 2632–2649.
[33] N. Zhang, R. Ciriminna, M. Pagliaro, Y.-J. Xu, *Chem. Soc. Rev.* **2014**, *43*, 5276–5287.
[34] M. Fujihira, Y. Satoh, T. Osa, *Nature* **1981**, *293*, 206–208.
[35] X.-Y. Zhang, H.-P. Li, X.-L. Cui, Y. Lin, *J. Mater. Chem.* **2010**, *20*, 2801–2806.
[36] N. Zhang, S. Liu, X. Fu, Y.-J. Xu, *J. Phys. Chem. C* **2011**, *115*, 9136–9145.
[37] X. Pan, M.-Q. Yang, X. Fu, N. Zhang, Y.-J. Xu, *Nanoscale* **2013**, *5*, 3601–3614.
[38] S. G. Kumar, L. G. Devi, *J. Phys. Chem. A* **2011**, *115*, 13211–13241.
[39] B. Y. Xia, B. Wang, H. B. Wu, Z. Liu, X. Wang, X. W. Lou, *J. Mater. Chem.* **2012**, *22*, 16499–16505.
[40] Y.-J. Xu, Y. Zhuang, X. Fu, *J. Phys. Chem. C* **2010**, *114*, 2669–2676.
[41] M.-Q. Yang, N. Zhang, M. Pagliaro, Y.-J. Xu, *Chem. Soc. Rev.* **2014**, *43*, 8240–8254.
[42] N. Zhang, Y. Zhang, Y.-J. Xu, *Nanoscale* **2012**, *4*, 5792–5813.
[43] Q. Xiang, J. Yu, M. Jaroniec, *Chem. Soc. Rev.* **2012**, *41*, 782–796.
[44] G. Williams, B. Seger, P. V. Kamat, *ACS Nano* **2008**, *2*, 1487–1491.
[45] N. Zhang, M.-Q. Yang, Z.-R. Tang, Y.-J. Xu, *ACS Nano* **2014**, *8*, 623–633.
[46] C. Han, M.-Q. Yang, N. Zhang, Y.-J. Xu, *J. Mater. Chem. A* **2014**, *2*, 19156–19166.
[47] C. Han, M.-Q. Yang, B. Weng, Y.-J. Xu, *Phys. Chem. Chem. Phys.* **2014**, *16*, 16891–16903.
[48] M.-Q. Yang, Y.-J. Xu, *Phys. Chem. Chem. Phys.* **2013**, *15*, 19102–19118.
[49] N. Zhang, Y.-J. Xu, *Chem. Mater.* **2013**, *25*, 1979–1988.
[50] L.-Y. Chen, Z.-D. Zhang, W.-Z. Wang, *J. Phys. Chem. C* **2008**, *112*, 4117–4123.
[51] X. Li, B. Weng, N. Zhang, Y.-J. Xu, *RSC Adv.* **2014**, *4*, 64484–64493.
[52] M.-Q. Yang, B. Weng, Y.-J. Xu, *J. Mater. Chem. A* **2014**, *2*, 1710–1720.
[53] X. An, J. C. Yu, F. Wang, C. Li, Y. Li, *Appl. Catal. B* **2013**, *129*, 80–88.
[54] Y. Zhang, Z.-R. Tang, X. Fu, Y.-J. Xu, *ACS Nano* **2010**, *4*, 7303–7314.
[55] N. Zhang, Y. Zhang, M.-Q. Yang, Z.-R. Tang, Y.-J. Xu, *J. Catal.* **2013**, *299*, 210–221.
[56] N. Zhang, M.-Q. Yang, Z.-R. Tang, Y.-J. Xu, *J. Catal.* **2013**, *303*, 60–69.
[57] M.-Q. Yang, N. Zhang, Y.-J. Xu, *ACS Appl. Mater. Interfaces* **2013**, *5*, 1156–1164.
[58] F.-X. Xiao, J. Miao, B. Liu, *J. Am. Chem. Soc.* **2014**, *136*, 1559–1569.
[59] Y. Zhang, N. Zhang, Z.-R. Tang, Y.-J. Xu, *ACS Nano* **2012**, *6*, 9777–9789.
[60] N. Zhang, Y. Zhang, X. Pan, M.-Q. Yang, Y.-J. Xu, *J. Phys. Chem. C* **2012**, *116*, 18023–18031.
[61] Y. Zhang, Z.-R. Tang, X. Fu, Y.-J. Xu, *ACS Nano* **2011**, *5*, 7426–7435.
[62] M.-Q. Yang, X. Pan, N. Zhang, Y.-J. Xu, *CrystEngComm* **2013**, *15*, 6819–6828.
[63] X. Chen, G. Wu, J. Chen, X. Chen, Z. Xie, X. Wang, *J. Am. Chem. Soc.* **2011**, *133*, 3693–3695.
[64] M. Zhang, C. Chen, W. Ma, J. Zhao, *Angew. Chem. Int. Ed.* **2008**, *47*, 9730–9733; *Angew. Chem.* **2008**, *120*, 9876–9879.
[65] M. Zhang, Q. Wang, C. Chen, L. Zang, W. Ma, J. Zhao, *Angew. Chem. Int. Ed.* **2009**, *48*, 6081–6084; *Angew. Chem.* **2009**, *121*, 6197–6200.
[66] N. Zhang, Y. Zhang, X. Pan, X. Fu, S. Liu, Y.-J. Xu, *J. Phys. Chem. C* **2011**, *115*, 23501–23511.
[67] K. S. W. Sing, D. H. Everett, R. A. W. Haul, L. Moscou, R. A. Pierotti, J. Rouquérol, T. Siemieniewska, *Pure Appl. Chem.* **1985**, *57*, 603–619.
[68] A. Mukherji, B. Seger, G. Q. Lu, L. Wang, *ACS Nano* **2011**, *5*, 3483–3492.
[69] Y. T. Liang, B. K. Vijayan, O. Lyandres, K. A. Gray, M. C. Hersam, *J. Phys. Chem. Lett.* **2012**, *3*, 1760–1765.
[70] W. Tu, Y. Zhou, Q. Liu, Z. Tian, J. Gao, X. Chen, H. Zhang, J. Liu, Z. Zou, *Adv. Funct. Mater.* **2012**, *22*, 1215–1221.
[71] Y. T. Liang, B. K. Vijayan, K. A. Gray, M. C. Hersam, *Nano Lett.* **2011**, *11*, 2865–2870.
[72] T. Lu, Y. Zhang, H. Li, L. Pan, Y. Li, Z. Sun, *Electrochim. Acta* **2010**, *55*, 4170–4173.
[73] H.-L. Guo, X.-F. Wang, Q.-Y. Qian, F.-B. Wang, X.-H. Xia, *ACS Nano* **2009**, *3*, 2653–2659.
[74] Y. Zhang, N. Zhang, Z.-R. Tang, Y.-J. Xu, *Chem. Sci.* **2013**, *4*, 1820–1824.
[75] Y. Zhang, N. Zhang, Z.-R. Tang, Y.-J. Xu, *Chem. Sci.* **2012**, *3*, 2812–2822.
[76] Q. Wang, M. Zhang, C. Chen, W. Ma, J. Zhao, *Angew. Chem. Int. Ed.* **2010**, *49*, 7976–7979; *Angew. Chem.* **2010**, *122*, 8148–8151.
[77] H. B. Michaelson, *J. Appl. Phys.* **1977**, *48*, 4729–4733.

Received: January 5, 2015
Revised: February 8, 2015

Duality is part of life: Ternary In_2S_3–(reduced graphene oxide–palladium) composites show enhanced visible-light photoactivity with the introduction of palladium nanoparticles, which act as dual cocatalyst with reduced graphene oxide.

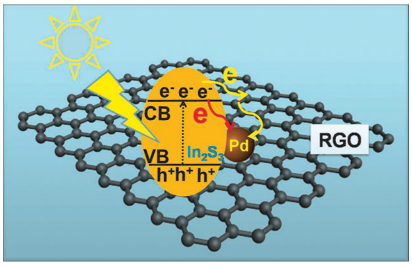

X. Li, N. Zhang, Y.-J. Xu*

■■ – ■■

Promoting Visible-Light Photocatalysis with Palladium Species as Cocatalyst